Supplement of

Sediment characteristics regulate anaerobic oxidation of methane coupled with nitrate and nitrite in the hyporheic zone

Yujia Wang et al.

Correspondence to: Florian Einsiedl (f.einsiedl@tum.de)

S1: Stream water data and sampling details

Due to the absence of a hydrological station at the Mühlangergraben, flow and water temperature data are sourced from the Moosach station of the Bavarian State Office for the Environment, located approximately 4 kilometers downstream. Since the Mühlangergraben is directly fed by the Moosach, the daily and annual fluctuations in flow rate and water temperature may generally mirror the dynamics of the small artificial stream. In 2024, the average annual discharge reached 3.7 $m^3 s^{-1}$, significantly exceeding the range of 1.6 to 2.4 $m^3 s^{-1}$ recorded from 2016 to 2023. Conversely, in 2025, the average annual discharge declined to approximately 2.45 $m^3 s^{-1}$, aligning with values at the upper end of the range from 2016 to 2023. Due to its predominantly straight planar shape and the absence of contraction areas, the water flow velocity exhibits minimal variation along its course of Mühlangergraben. Consequently, the hydraulic boundary conditions in this section of the river are relatively uniformly distributed. Water temperature displayed a typical seasonal pattern, with daily minimum around 5.3 °C in January, followed by a gradual increase leading into summer. Detailed information on stream discharge as well as surface water temperatures during the sampling period is given in Fig. S1.

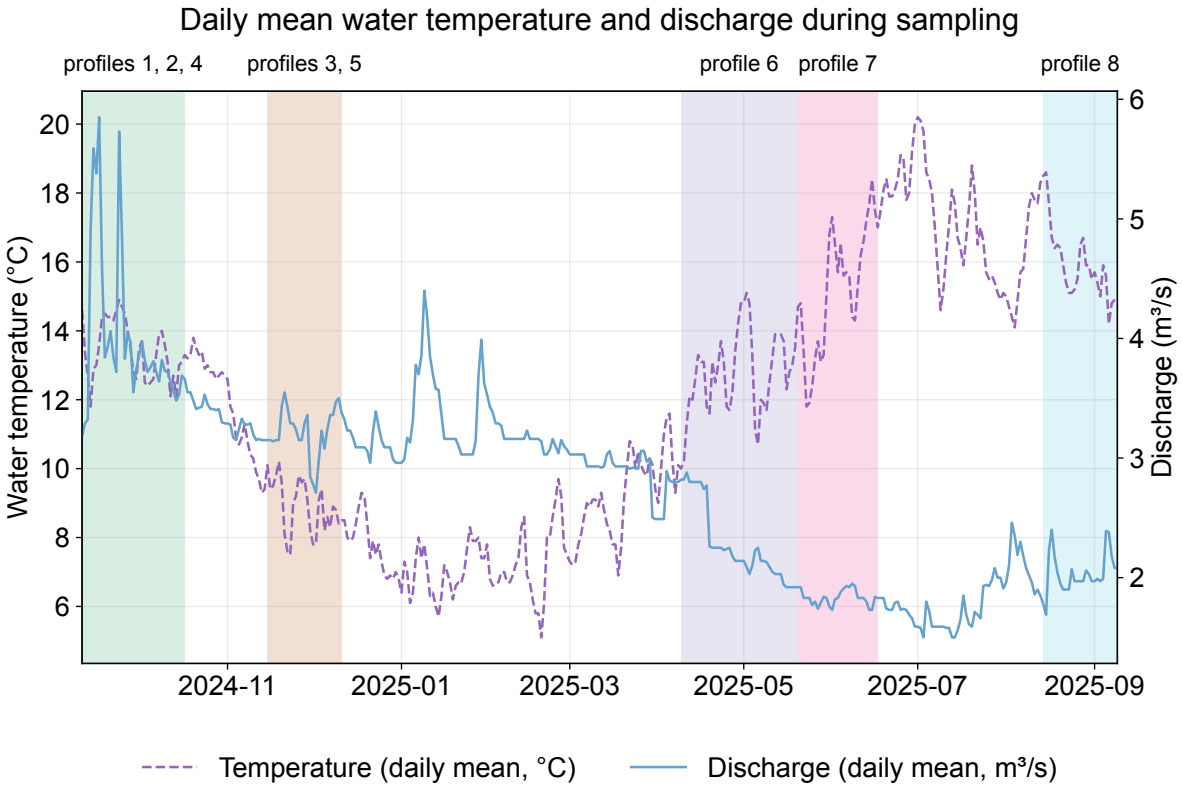

Figure S1: Stream water temperature (daily mean) und discharge from 11 September 2024 to 09 September 2025. Data was recorded at gauging station Freising Moosach (river chainage: 9.45 km, 4.5 km downstream of the sampling sites), as retrieved from the Bavarian State Office for the Environment.

Tab. S1 presents the sampling details, encompassing the sampling equipment, pore water sampling intervals, and surface water characteristics, including water temperature, dissolved oxygen, pH, and conductivity.

Table S1. Deployment and sampling overview of hyporheic zone porewater profiles

Profile	Location	Sampling Equipment	Placement date	Sampling date	Days	Tsw (°C)	O_2 (mg L^{-1})	pH	Conductivity (µS cm^{-1})
1	A	peeper-type1	2024-09-11	2024-10-17	36	13.9	7.94	9.815	747
2	B	peeper-type1	2024-09-11	2024-10-17	36	13.9	7.94	9.815	747
3	B	peeper-type1	2024-11-15	2024-12-11	26	8.8	11.39	8.126	778
4	C	peeper-type1	2024-09-11	2024-10-17	36	13.3	8.41	9.322	767
5	C	peeper-type1	2024-11-15	2024-12-11	26	8.7	11.40	8.257	766
6	D	peeper-type1	2025-04-09	2025-05-20	42	13.5	8.68	7.534	767
7	D	peeper-type2	2025-05-20	2025-06-17	29	15.0	9.25	7.822	754
8	D	peeper-type1	2025-08-14	2025-09-09	27	14.8	9.07	7.995	768

S2: Sediment characteristic and sieving analysis

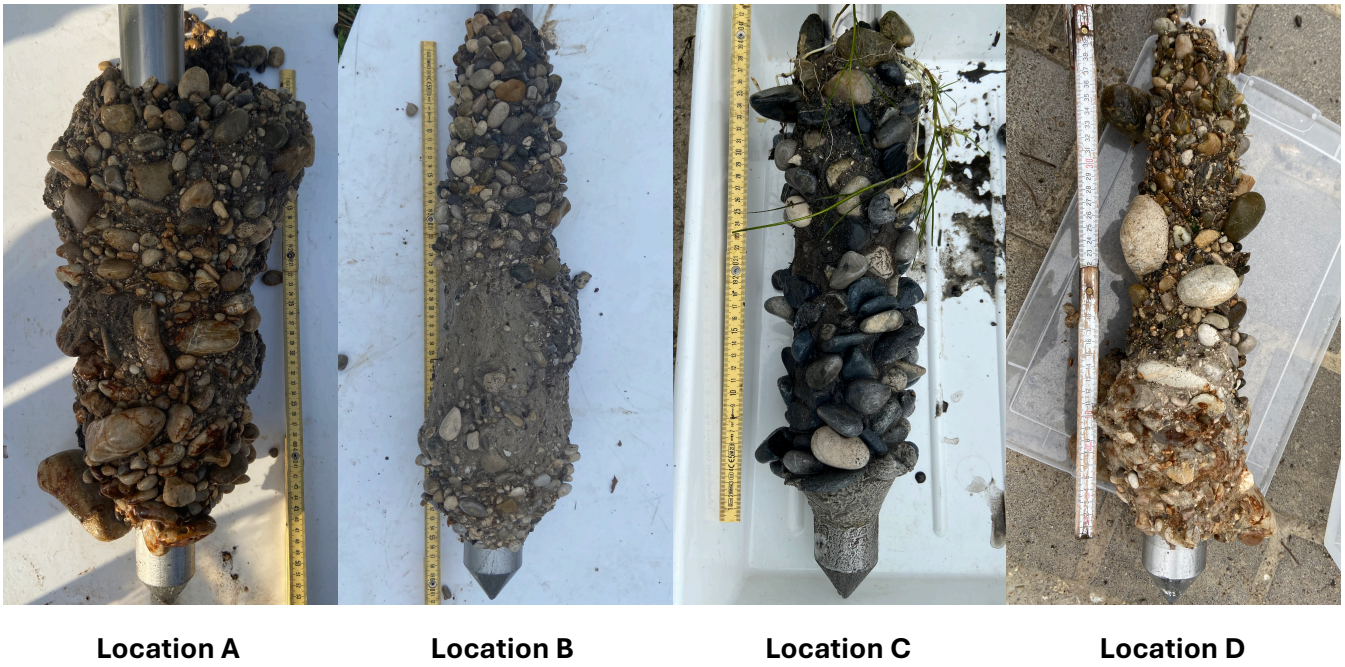

Figure S2: Freeze-core sediment cores illustrating structural differences among locations A-D

Fig. S2 presents freeze-core sediment samples collected from the four study locations (A-D), arranged from left to right. The samples illustrate pronounced spatial variability in sediment structure and composition across the study sites. It should be

noted that the freeze-core method may lead to partial loss of bound material during extraction, therefore, the samples shown here provide a representative, but not fully preserved, depiction of in situ sediment characteristics. Sediments from Locations A and D originate from natural, unmodified riverbeds and exhibit highly heterogeneous structures. The cores contain a wide range of grain sizes, including clay, silt, fine to coarse sand, gravel, and stones, which are irregularly mixed and interlocked without a clearly dominant fraction. This results in a poorly sorted and structurally complex sediment matrix. At Location B, a distinct anthropogenic interface is visible at approximately 20 cm depth. Above this boundary, the sediment is dominated by relatively well-sorted medium gravel (8-16 mm), forming a uniform and coarse-grained layer. Below this interface, the sediment transitions into a finer-grained matrix, where clay-rich material is interspersed with scattered gravel particles, resulting in a more compact and heterogeneous structure. At Location C, the sediment is predominantly composed of coarse gravel (16-32 mm) that appears relatively well organized and closely packed. However, closer inspection shows the presence of fine sediments interspersed within the gravel framework, indicating partial infilling of pore spaces despite the overall coarse-grained structure.

Sediment grain-size distributions were determined by sieve analysis following DIN EN ISO 17892-4. Before sieving, samples were oven-dried at 110 ± 5 °C and weighed. Fine material (silt and clay fractions) was separated from the coarse fraction by wet sieving using a 0.063 mm mesh. The retained coarse fraction was subsequently dried and dry-sieved manually into defined grain-size classes. Sediment texture classes were assigned following DIN EN ISO 14688-1. Potential sources of uncertainty associated with sieve duration, vibration intensity, and limited sample mass were minimized by adhering to standardized procedures and quality criteria specified in DIN EN ISO 17892-4. The grain size distribution data listed in Tab. S2 and sorting characteristics listed in Tab. S3, which further served as the basis for subsequent calculations of sediment porosity.

Table S2. Grain-size composition of sediments

Location	Depth (cm)	Clay and Silt (%)	Sand			Gravel		
			Fine (%)	Medium (%)	Coarse (%)	Fine (%)	Medium (%)	Coarse (%)
B	0-16	0.0	0.0	0.0	0.0	0.3	97.7	2.0
	16-27	6.4	6.3	23.1	2.9	10.3	47.1	3.9
C	0-27	1.3	2.2	8.6	2.5	2.4	15.5	67.5

At location B, fine-grained and sandy fractions in the shallow sediment had been removed by hydrodynamic flushing, resulting in a homogeneous medium-gravel sample. For this uniform gravel, porosity was determined experimentally by a volumetric method. Oven-dried (110 ± 5 °C) gravel was placed into a cylindrical container (diameter 10 cm), and water was added until all pore spaces were completely saturated. Total volume was calculated from the measured sediment height, and porosity was defined as the ratio of water volume to total volume. For gravel-dominated sediments, effective porosity can be approximated by total porosity (Hölting and Coldewey, 2013).

For heterogeneous sediment samples from the lower part of location B and from location C, experimental porosity determination was not feasible due to fine-grained infilling. Instead, porosity (φ, dimensionless) was estimated using the empirical relationship proposed by Wu and Wang (2006), which depends solely on the median grain size d_{50} (mm), Eq. (S1):

$$\varphi = 0.13 + \frac{0.21}{(d_{50}+0.002)^{0.21}}, \quad \text{(S1)}$$

Table S3. Sorting characteristics derived from sieve analysis and porosity

Location	Depth interval (cm)	d_{10} (mm)	d_{25} (mm)	d_{50} (mm)	d_{60} (mm)	φ
B	0-16	8.00	9.30	11.40	12.40	0.4
	16-27	0.16	0.37	6.50	8.30	0.27
C	0-27	0.48	14.00	27.90	31.80	0.23

Hydraulic conductivity (K) was estimated from grain-size parameters using the empirical relationships proposed by Seiler (1973) for unconsolidated gravel-sand deposits. The coefficient of uniformity (C_u) was defined as $C_u = d_{60}/d_{10}$. Depending on C_u, two different formulations were applied. For sediments with moderate sorting ($5 < C_u < 17$), hydraulic conductivity was calculated using Eq. (S2), whereas for poorly sorted sediments ($17 < C_u < 100$), Eq. (S3) was applied. The correc factors $x_{10}(C_u)$ and $x_{25}(C_u)$ were obtained from Seiler (1973). Consequently, the resulting hydraulic conductivity values should be interpreted as first-order estimates rather than precise representations of effective permeability.

$$K = \frac{x_{10}(C_u)}{1000} \cdot d_{10}^2, \quad \text{(S2)}$$

$$K = \frac{x_{25}(C_u)}{1000} \cdot d_{25}^2, \quad \text{(S3)}$$

Sediment permeability (k) was subsequently calculated from hydraulic conductivity using the relationship between permeability and fluid properties following Shipley et al. (1997). Hydraulic conductivity and sediment permeability are related through Eq. (S4), which can be rearranged to Eq. (S5) for calculating k.

$$K = \frac{k\rho g}{\mu}, \quad \text{(S4)}$$

$$k = \frac{K\mu}{\rho g}, \quad \text{(S5)}$$

In these calculations, gravitational acceleration was set to g = 9.8 m s^{-2}. Fluid properties were assigned according to water temperature at each location. For Location B (13.9 °C), a water density of ρ = 999.26 kg m^{-3} and a dynamic viscosity of μ = 1.169 × 10^{-3} Pa s were used. For Location C (13.3 °C), a water density of ρ = 999.34 kg m^{-3} and a dynamic viscosity of μ = 1.188 × 10^{-3} Pa s were applied. The calculated results are summarized in Tab. S4.

Table S4. Estimated hydraulic conductivity and sediment permeability

Location	Depth interval (cm)	C_u (-)	Correction factor (-)	K (m/s)	k (m²)
B	0–16	1.55	21.5*	1.38	1.64×10^{-7}
	16–27	51.88	1.0	1.37×10^{-4}	1.63×10^{-11}
C	0–27	66.25	2.98	5.84×10^{-1}	7.08×10^{-8}

* For Location B (0–16 cm), $C_u < 5$, the correction factor for $C_u = 5$ was applied as a lower-bound approximation.

The LOI results for locations B and C are shown in Fig. S3

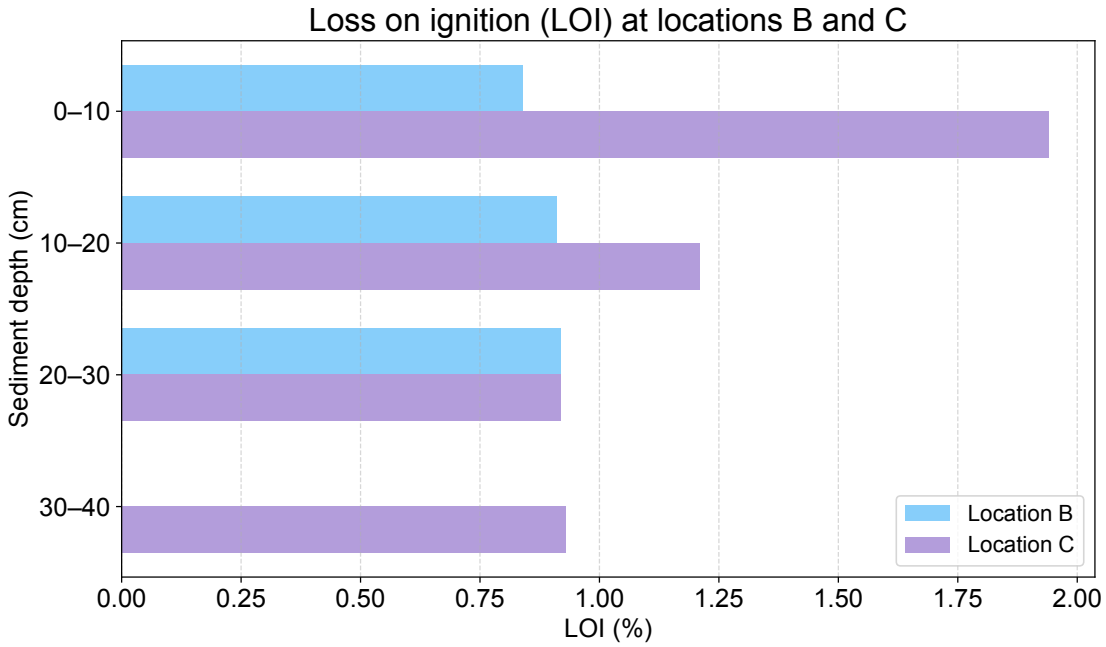

Figure S3: Loss on ignition (LOI) at locations B and C

S3: Effective molecular diffusion coefficients (D_s)

To parameterize diffusion-controlled transport in PROFILE, effective molecular diffusion coefficients in sediments (D_s) were derived from molecular diffusion coefficients in free water (D_0) and corrected for porosity-related tortuosity. Because the mean water temperature during the sampling interval was identical for profiles B and C, the same D_0 values were applied to both profiles.

For dissolved gases (O_2), D_0 was calculated following Boudreau (1997) as:

$$D_0 = 4.72 \times 10^{-9} \frac{T}{\mu V_b^{0.6}}, \quad \text{(S6)}$$

where T is absolute temperature (K), μ is the dynamic viscosity of water (P), and V_b is the molar volume of the dissolved gas ($cm^3\ mol^{-1}$). In this study, μ was set to 0.011867 P, molar volumes (V_b) were taken from the PROFILE parameter set and set to 27.9 $cm^3\ mol^{-1}$ for O_2.

For dissolved ions (NO_3^- and SO_4^{2-}), D_0 follows an empirical linear temperature relationship Boudreau (1997):

$$D_0 = (m_0 + m_1\, t) \times 10^{-6}, \quad \text{(S7)}$$

where t is temperature (°C) and m_0, m_1 are ion-specific constants taken from the literature/PROFILE parameter set. Table S5 lists the D_0 values. In the study, the constants were adopted from the PROFILE model parameter set, with $m_0 = 9.50$ and $m_1 = 0.388$ for NO_3^- , and $m_0 = 4.88$ and $m_1 = 0.232$ for SO_4^{2-}, respectively.

Sediment diffusion coefficients were then obtained using the Iversen and Jørgensen (1993) relationship implemented in PROFILE:

$$D_s = \frac{D_0}{1+n(1-\varphi)}, \quad \text{(S8)}$$

where φ is sediment porosity and n are an empirical constant fixed to 3 in PROFILE (Version 1.0). Site-specific porosities were $\varphi_{B,0\text{-}16} = 0.40$ and $\varphi_{B,under\ 16} = 0.27$ for profile B and $\varphi_C = 0.23$ for profile C. Resulting D_s values used as model input are summarized in Tab. S6.

Table S5. Molecular diffusion coefficients in free water (D_0)

Solute	Profile	D_0 ($m^2\ s^{-1}$)
O_2	B and C	1.55×10^{-9}
NO_3^-	B and C	1.47×10^{-9}
SO_4^{2-}	C	8.00×10^{-10}

Table S6. Effective sediment diffusion coefficients (D_s)

Solute	Profile	Porosity φ (-)	D_s ($m^2\ s^{-1}$)
O_2	B 0-16 cm	0.40	5.54×10^{-10}
	B 16-27cm	0.27	4.86×10^{-10}
NO_3^-	B 0-16 cm	0.40	5.25×10^{-10}
	B16-27 cm	0.27	4.61×10^{-10}

O_2	C	0.23	4.68×10^{-10}
NO_3^-	C	0.23	4.61×10^{-10}
SO_4^{2-}	C	0.23	2.42×10^{-10}

S4: Details and results of the 1D reactive transport model implemented in PHREEQC

Microbial biomass concentrations X used in the Monod-type kinetic expressions were derived from depth-resolved 16S rRNA gene copy numbers and the relative abundance measured in wet sediment samples with high-resolution. Microbial functional groups associated with the four modeled methane transformation pathways were assigned based on site-specific community composition data. Aerobic methane oxidation (MOx) was attributed to canonical aerobic methanotrophs. The nitrate-dependent anaerobic methane oxidation pathway (NO_3^--DAMO) was represented by microorganisms related to *Crenothrix*, which have been suggested to couple methane oxidation to nitrate reduction under low-oxygen conditions. The nitrite-dependent anaerobic methane oxidation pathway (NO_2^--DAMO) was assigned to members of the NC10 phylum, such as *Candidatus Methylomirabilis*, which are known to oxidize methane using nitrite via an intra-aerobic pathway. Denitrification (DENI) was attributed to heterotrophic denitrifying bacteria capable of reducing nitrate to nitrite and further to gaseous nitrogen species. The relative abundance of these microbial groups and their spatial distribution were derived from sequencing data obtained at location C, specifically from the 0-9 cm sediment interval, as presented in Fig. 5a, c, d and Fig. S4. These data were converted to biomass per unit pore-water volume to ensure consistency with the aqueous-phase reaction kinetics implemented in the PHREEQC reactive transport model.

Microbial biomass X_k (g L^{-1} pore water) was calculated from gene copy numbers according to Eq. (S9):

$$X_k = \frac{N_{16S,tot} \cdot f_k \cdot \rho_{wet} \cdot \frac{m_{cell}}{f_C} \cdot 1000}{\phi \cdot n_{16S}}, \quad \text{(S9)}$$

where $N_{16S,tot}$ is the total 16S rRNA gene copy number determined by qPCR (copies g^{-1} wet sediment), f_k is the relative abundance of functional group k derived from 16S rRNA gene sequencing (-), ρ_{wet} is the wet bulk density of sediment (g cm^{-3}), m_{cell} is the average cellular carbon mass (g $cell^{-1}$), f_c denotes the carbon mass fraction of microbial biomass (-), n_{16S} is the average number of 16S rRNA gene copies per cell (copies $cell^{-1}$), and φ is sediment porosity (-).

The following parameter values were used: ρ_{wet} = 1.37 g cm^{-3} (Pepers et al., 2024), $m_{cell} = 2.0 \times 10^{-14}$ g $cell^{-1}$ (Lapoussière et al., 2011; Fagerbakke et al., 1996), n_{16S} = 3.04 copies $cell^{-1}$ (Větrovský and Baldrian, 2013), f_c = 50 % (Cermak et al., 2017), φ = 0.23. The results are presented in Tab. S7.

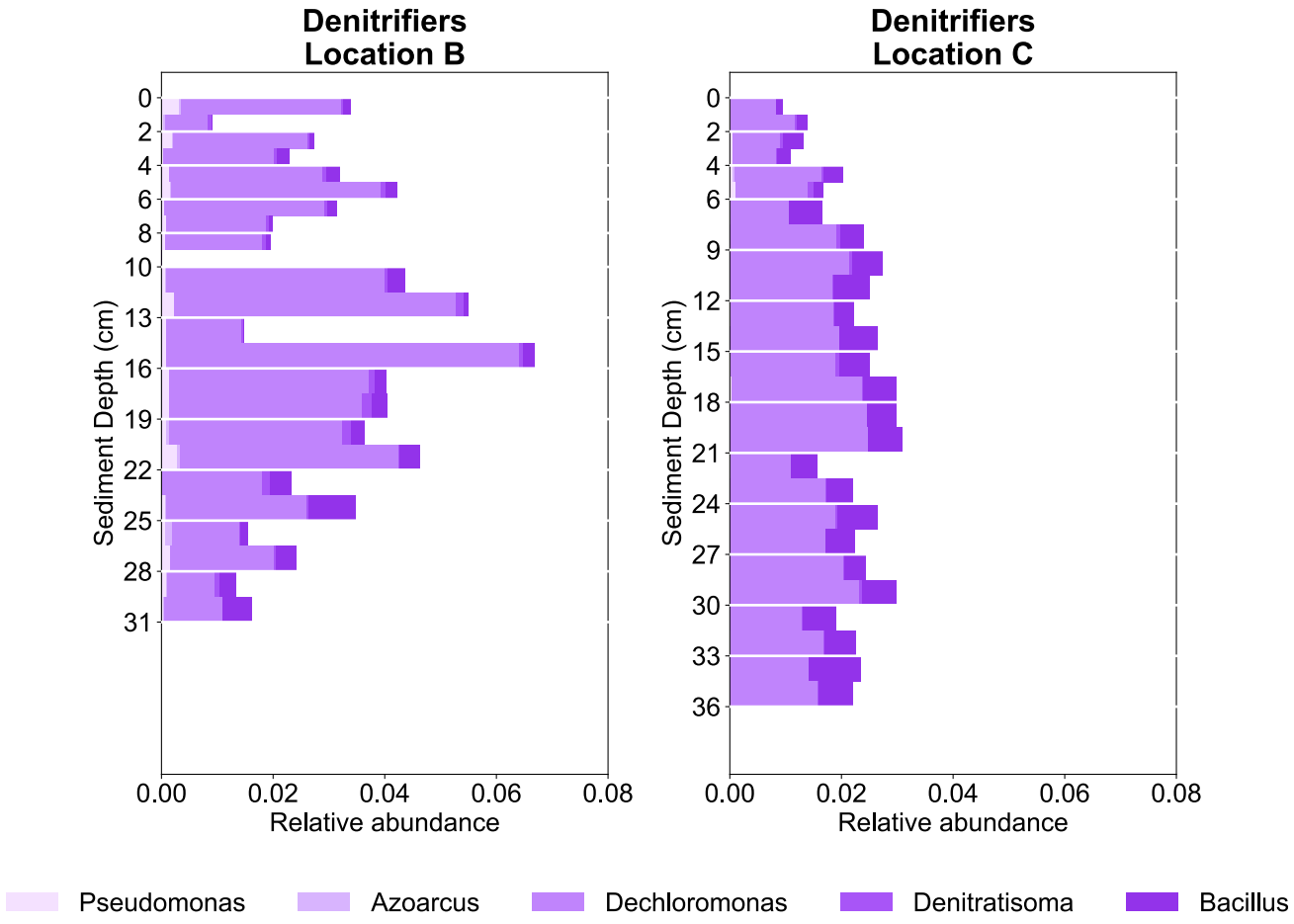

Figure S4: The relative abundance of denitrifiers based on the sediment depth at locations B and C

Table S7. Prescribed microbial biomass values X (g L^{-1} pore water) used in the model

Depth interval (cm)	X_{MOx}	$X_{NO3\text{-}DAMO}$	$X_{NO2\text{-}DAMO}$	X_{DENI}
0-2	0.001486	0.000318	0.0000515	0.0004865
2-4	0.000972	0.000250	0.0000315	0.0003373
4-6	0.000465	0.000196	0.0000825	0.0003845
6-9	0.000694	0.0000308	0.0000301	0.0004567

The maximum rate constant (μ), half-saturation constant (Ks), and yield coefficient (Y) were adopted from published literature values for the reaction processes. In contrast, the active fraction (f_a) was treated as a fitting parameter to represent the proportion of metabolically active biomass under in situ conditions. Detailed parameter values and their sources are provided in Tab. S8. The first-order rate constants (k) for oxygen and nitrate are listed in Tab. S9.

Table S8. Kinetic parameters used in Monod-type reaction rate expressions

Process	Parameter	Symbol	Value	Unit	Reference
MOx (aerobic methane oxidation)	Maximum rate constant	μ_{MOx}	2.0×10^{-6}	s^{-1}	Zimmermann et al., 2021
	Half-saturation constant (CH_4)	$K_{s,CH_4,MOx}$	0.02	mmol kg^{-1} w	Mayr et al., 2020
	Half-saturation constant (O_2)	K_{s,O_2}	0.06	mmol kg^{-1} w	Guérin and Abril, 2007
	Yield coefficient	Y_{MOx}	7.2×10^{-3}	g biomass $mmol^{-1}$ CH_4	Lee et al., 2024
	Active fraction	$f_{a,MOx}$	0.10	-	-
NO_3^--DAMO (nitrate-dependent anaerobic methane oxidation)	Maximum rate constant	$\mu_{NO_3\text{-}DAMO}$	1.4×10^{-6}	s^{-1}	Yu et al., 2017
	Half-saturation constant (CH_4)	K_{s,CH_4,NO_3}	0.08	mmol kg^{-1} w	Yu et al., 2017
	Half-saturation constant (NO_3^-)	K_{s,NO_3}	0.01	mmol kg^{-1} w	Delgado Vela et al., 2015
	Yield coefficient	$Y_{NO_3\text{-}DAMO}$	4.8×10^{-3}	g biomass $mmol^{-1}$ CH_4	Yu et al., 2017
	Active fraction	$f_{a,NO_3\text{-}DAMO}$	0.30	-	-
NO_2^--DAMO (nitrite-dependent anaerobic methane oxidation)	Maximum rate constant	$\mu_{NO_2\text{-}DAMO}$	4.1×10^{-7}	s^{-1}	Delgado Vela et al., 2015
	Half-saturation constant (CH_4)	K_{s,CH_4,NO_2}	0.005	mmol kg^{-1} w	Delgado Vela et al., 2015
	Half-saturation constant (NO_2^-)	K_{s,NO_2}	0.04	mmol kg^{-1} w	Delgado Vela et al., 2015
	Yield coefficient	$Y_{NO_2\text{-}DAMO}$	1.7×10^{-3}	g biomass $mmol^{-1}$ CH_4	Delgado Vela et al., 2015
	Active fraction	$f_{a,NO_2\text{-}DAMO}$	0.20	-	-
DENI (denitrification)	Maximum rate constant	μ_{DENI}	3.0×10^{-6}	s^{-1}	Foglar and Briški, 2003
	Half-saturation constant (NO_3^-)	$K_{s,NO_3,DENI}$	1.9×10^{-2}	mmol kg^{-1} w	Dinçer and Kargi, 2000
	Yield coefficient	Y_{DENI}	8.4×10^{-3}	g biomass $mmol^{-1}$ NO_3^-	Foglar and Briški, 2003
	Active fraction	$f_{a,DENI}$	0.20	-	-
	NO_2^- allocation fraction	f_{NO_2}	0.50	-	-

Table S9. First-order background sink parameters

Background process	Parameter	Symbol	Value	Unit
NO_3^- background process	First-order rate constant	$k_{NO_3,\,BG}$	6.0×10^{-6}	s^{-1}
O_2 background process	First-order rate constant	$k_{O_2,\,BG}$	2.6×10^{-6}	s^{-1}

The top and bottom boundary concentrations as well as the initial cell concentrations for CH_4, O_2, NO_3^-, and NO_2^- are provided in Tab. S10(a). Transport-related parameters, including diffusion, advection, and dispersion coefficients, are summarized in Tab. S10(b).

The effective diffusion coefficient of methane was derived using Fick's first law, $J = -D\frac{dC}{dx}$, with J represents the methane flux, calculated as the total mixed-gas flux collected at location C within the Profile 8 sampling interval multiplied by the methane concentration. The concentration gradient $\frac{dC}{dx}$ was determined from high-resolution porewater concentration profiles (1 cm resolution) by calculating the mean concentration difference over 2 cm intervals. Rearranging Fick's first law allowed estimation of the effective diffusion coefficient D, which was subsequently used as the methane effective diffusivity in the model. For O_2, NO_3^-, and NO_2^-, effective diffusion coefficients were calculated using the porosity correction relationship $D = D_w \cdot \varphi^n$, where D_w is the molecular diffusion coefficient obtained from the PHREEQC database, φ is porosity (0.23), and n was set to 1.

Table S10. Boundary conditions and transport parameters used in the reactive transport model

(a) Boundary conditions (concentrations)

Species	Top boundary (Cell 0)	Bottom boundary (Cell 9)	Initial concentration (Cells 1-8)	Unit
CH_4	0.8	136.96	0	μmol L^{-1}
O_2	262.81	9.70	0	μmol L^{-1}
NO_3^-	388.68	11.32	0	μmol L^{-1}
NO_2^-	3.05	3.05	0	μmol L^{-1}

(b) Transport parameters

Parameter	Symbol	Value	Unit	Reference
Porosity	φ	0.23	-	This study
Advective pore-water velocity	v	1.00×10^{-7}	m s^{-1}	This study
Longitudinal dispersivity	αL	0.0030	m	This study
Mechanical dispersion coefficient	D_{disp}	3.00×10^{-10}	m^2 s^{-1}	This study
Effective diffusion coefficient (CH_4)	D_{CH_4}	3.05×10^{-9}	m^2 s^{-1}	Fick's first law
Effective transport coefficient (O_2)	D_{O_2}	5.41×10^{-10}	m^2 s^{-1}	PHREEQC database
Effective transport coefficient (NO_3^-)	$D_{NO_3^-}$	4.37×10^{-10}	m^2 s^{-1}	PHREEQC database
Effective transport coefficient (NO_2^-)	D_{NO2^-}	4.39×10^{-10}	m^2 s^{-1}	PHREEQC database

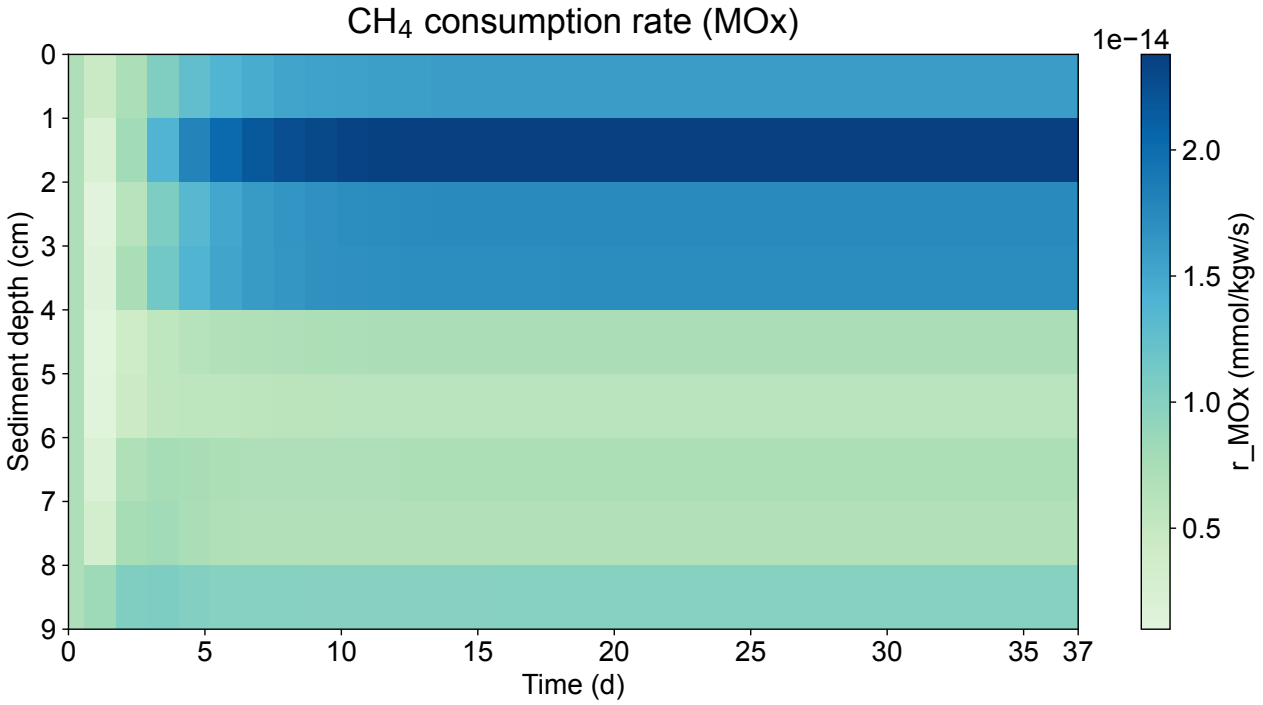

Figure S5: Methane consumption rate over time and depth under the aerobic methane oxidation pathway

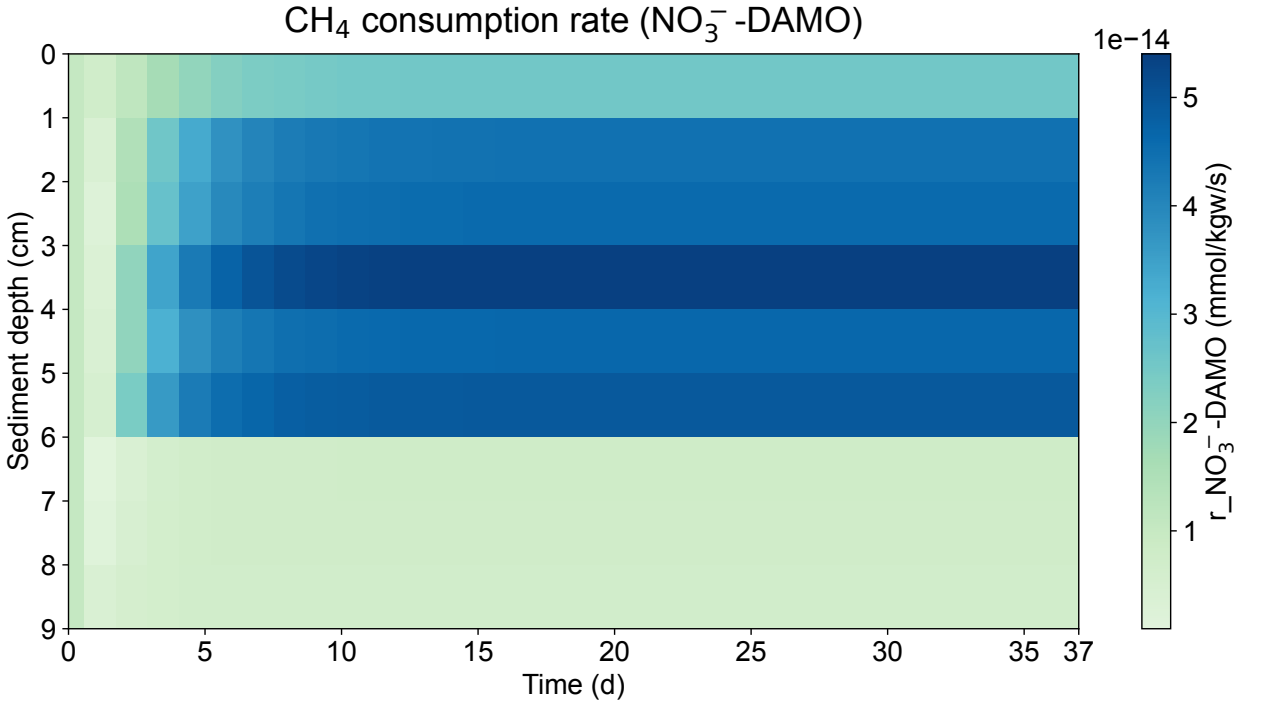

Figure S6: Methane consumption rate over time and depth under the nitrate-dependent anaerobic methane oxidation pathway

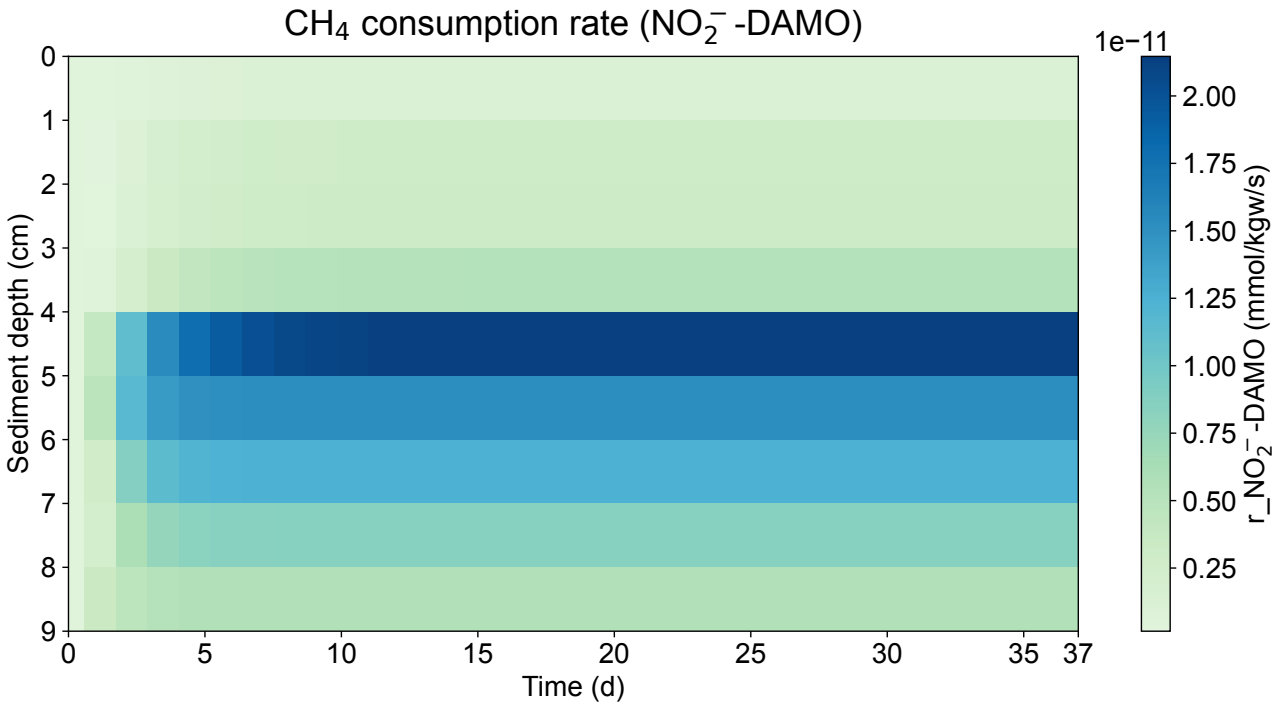

Figure S7: Methane consumption rate over time and depth under the nitrite-dependent anaerobic methane oxidation pathway

References

Bavarian State Office for the Environment: Gewässerkundlicher Dienst Bayern, https://www.gkd.bayern.de/en/, 2025.

Boudreau, B. P.: Diagenetic Models and Their Implementation, Springer Berlin Heidelberg, Berlin, Heidelberg, 1997.

Cermak, N., Becker, J. W., Knudsen, S. M., Chisholm, S. W., Manalis, S. R., and Polz, M. F.: Direct single-cell biomass estimates for marine bacteria via Archimedes' principle, The ISME journal, 11, 825–828, https://doi.org/10.1038/ismej.2016.161, 2017.

Delgado Vela, J., Stadler, L. B., Martin, K. J., Raskin, L., Bott, C. B., and Love, N. G.: Prospects for Biological Nitrogen Removal from Anaerobic Effluents during Mainstream Wastewater Treatment, Environ. Sci. Technol. Lett., 2, 234–244, https://doi.org/10.1021/acs.estlett.5b00191, 2015.

Dinçer, A. R. and Kargi, F.: Kinetics of sequential nitrification and denitrification processes, Enzyme and microbial technology, 27, 37–42, https://doi.org/10.1016/S0141-0229(00)00145-9, 2000.

Fagerbakke, K. M., Heldal, M., and Norland, S.: Content of carbon, nitrogen, oxygen, sulfur and phosphorus in native aquatic and cultured bacteria, Aquat. Microb. Ecol., 10, 15–27, https://doi.org/10.3354/ame010015, 1996.

Foglar, L. and Briški, F.: Wastewater denitrification process—the influence of methanol and kinetic analysis, Process Biochemistry, 39, 95–103, https://doi.org/10.1016/S0032-9592(02)00318-7, 2003.

Guérin, F. and Abril, G.: Significance of pelagic aerobic methane oxidation in the methane and carbon budget of a tropical reservoir, J. Geophys. Res., 112, https://doi.org/10.1029/2006JG000393, 2007.

Hölting, B. and Coldewey, W. G.: Hydrogeologie, Springer Berlin Heidelberg, Berlin, Heidelberg, 2013.

Iversen, N. and Jørgensen, B. B.: Diffusion coefficients of sulfate and methane in marine sediments: Influence of porosity, Geochimica et Cosmochimica Acta, 57, 571–578, https://doi.org/10.1016/0016-7037(93)90368-7, 1993.

Lapoussière, A., Michel, C., Starr, M., Gosselin, M., and Poulin, M.: Role of free-living and particle-attached bacteria in the recycling and export of organic material in the Hudson Bay system, Journal of Marine Systems, 88, 434–445, https://doi.org/10.1016/j.jmarsys.2010.12.003, 2011.

Lee, S. A., Henard, J. M., Alba, R. A. C., Benedict, C. A., Mayes, T. A., and Henard, C. A.: Overexpression of native carbonic anhydrases increases carbon conversion efficiency in the methanotrophic biocatalyst Methylococcus capsulatus Bath, mSphere, 9, e0049624, https://doi.org/10.1128/msphere.00496-24, 2024.

Mayr, M. J., Zimmermann, M., Dey, J., Wehrli, B., and Bürgmann, H.: Lake mixing regime selects apparent methane oxidation kinetics of the methanotroph assemblage, Biogeosciences, 17, 4247–4259, https://doi.org/10.5194/bg-17-4247-2020, 2020.

Pepers, K. H. J., van Egmond, F., Koomans, R., Teuling, K., Staats, G., and van Os, G.: Validation of a new gamma ray soil bulk density sensor, European J Soil Science, 75, https://doi.org/10.1111/ejss.13542, 2024.

Seiler, K.-P.: Durchlässigkeit, Porosität und Kornverteilung quartärer Kies-Sand-Ablagerungen des bayerischen Alpenvorlandes, GWF Wasser Abwasser 114, 353–400, 1973.

Shipley, T. H., Ogawa, Y., Blum, P., and Bahr, J. M. (Eds.): Proceedings of the Ocean Drilling Program, 156 Scientific Results, Proceedings of the Ocean Drilling Program, Ocean Drilling Program, 1997.

Větrovský, T. and Baldrian, P.: The variability of the 16S rRNA gene in bacterial genomes and its consequences for bacterial community analyses, PloS one, 8, e57923, https://doi.org/10.1371/journal.pone.0057923, 2013.

Wu, W. and Wang, S. S. Y.: Formulas for Sediment Porosity and Settling Velocity, J. Hydraul. Eng., 132, 858–862, https://doi.org/10.1061/(ASCE)0733-9429(2006)132:8(858), 2006.

Yu, H., Kashima, H., Regan, J. M., Hussain, A., Elbeshbishy, E., and Lee, H.-S.: Kinetic study on anaerobic oxidation of methane coupled to denitrification, Enzyme and microbial technology, 104, 47–55, https://doi.org/10.1016/j.enzmictec.2017.05.005, 2017.

Zimmermann, M., Mayr, M. J., Bürgmann, H., Eugster, W., Steinsberger, T., Wehrli, B., Brand, A., and Bouffard, D.: Microbial methane oxidation efficiency and robustness during lake overturn, https://doi.org/10.3929/ethz-b-000509323, 2021.